NMR Structure of Lung Surfactant Peptide SP-B_{11-25}

Josh W. Kurutz† and Ka Yee C. Lee*

Department of Chemistry, Institute for Biophysical Dynamics, and James Franck Institute, University of Chicago, 5735 S. Ellis Ave., Chicago, Illinois 60637

Received December 20, 2001; Revised Manuscript Received April 15, 2002

ABSTRACT: Surfactant protein B (SP-B) is a 79-residue essential component of lung surfactant, the film of lipid and protein lining the alveoli, and is the subject of great interest for its role in lung surfactant replacement therapies. Here we report circular dichroism results and the solution NMR structure of SP-B_{11-25} (CRALIKRIQAMIPKG) dissolved in CD_3OH at 5 °C. This is the first report of NMR data related to the protein SP-B, whose structure promises to help elucidate the mechanism of its function. Sequence-specific resonance assignments were made for all observable ^1H NMR signals on the basis of standard 2D NMR methods. Structures were determined by the simulated annealing method using restraints derived from 2D NOESY data. The calculations yielded 17 energy-minimized structures, three of which were subjected to 0.95 ns of restrained dynamics to assess the relevance of the static structures to more realistic dynamic behavior. Our CD and NMR data confirm that this segment is an amphiphilic α helix from approximately residue L14 through M21. The backbone heavy-atom RMSD for residues L14 through M21 is 0.09 ± 0.12 Å, and the backbone heavy-atom RMSD for the whole peptide is 0.96 ± 2.45 Å, the difference reflecting fraying at the termini. Aside from the disordered termini, the minimized structures represent dynamic structures well. Structural similarity to the homologous regions of related saposin-like proteins and the importance of the distribution of polar residues about the helix axis are discussed.

Surfactant protein B (SP-B[1]) (*1*) is an essential component of mammalian lung surfactant (LS), a complex mixture of lipids and proteins that lines the alveoli (*2*). LS reduces surface tension at the air−water interface, thus preventing alveolar collapse and reducing the work of breathing (*3*−*5*). Infants born prematurely often lack LS (*6*) and consequently suffer from neonatal respiratory distress syndrome (NRDS), which has been treated with surfactant replacement therapy since 1989 (*7*−*9*). Formulation of replacement LS has focused on reproducing the composition and surface tension-lowering properties of the natural substance by combining pure lipids, purifying surfactant extracts from cows or pigs, or adding isolated surfactant proteins from animals to mixtures of pure lipids (*10*). Therapeutic surfactants containing surfactant proteins (*11*) are clinically preferred and perform better in in vitro experiments, but the specific functions of the proteins and their structure−function relationships are not well understood (*10*, *12*−*14*). Of the four LS proteins, surfactant proteins A, B, C, and D (SP-A, -B, -C, and -D), SP-B and SP-C are more important for LS replacements (*8*, *9*, *15*, *16*). SP-A and SP-D are involved primarily in immunological functions, though their interactions with SP-B and SP-C may be critical for surfactant homeostasis in healthy individuals (*2*, *11*). SP-B and SP-C are both hydrophobic and exhibit high surface activities (*1*, *17*). We focus our attention on SP-B because it is the major protein in commercial LS replacements (*9*, *10*) and because it is critical to mammalian survival (*18*, *19*): mice lacking the SP-B gene die shortly after birth (*20*), whereas those lacking SP-C continue to live, albeit impaired (*21*).

Though SP-B is important for surfactant function, its role in LS and its important structural features are unclear. In LS, SP-B is a disulfide-linked homodimer of 79-residue monomers, each of which features four putative α helices and is predicted to be amphiphilic (*1*, *22*). Its effects on lipid monolayers in Langmuir monolayer studies show that SP-B reduces the minimum surface tension achieved on compression and enhances the ability of collapsed lipid films to rapidly respread on the air−water interface (*23*−*27*). A great deal of attention has been focused on the N-terminal 25-residue segment of SP-B, SP-B_{1-25}, which faithfully reproduces the functional aspects of the full-length protein, contains no disulfide bonds, and is more amenable to chemical synthesis than the full-length protein (*28*−*31*). SP-B and SP-B_{1-25} induce lipid films to fold reversibly when compressed, which provides a unique model for why SP-B is essential for human health (*25*, *27*). The SP-B_{1-25} peptide is proposed to comprise three regions: an N-terminal sequence of approximately 10 hydrophobic residues, termed the insertion sequence, an amphiphilic α helical region from the insertion sequence to P23, and a disordered C-terminus.

We are particularly interested in the functional role of the approximately 10-residue N-terminal hydrophobic tail, which

* Corresponding author. E-mail: kayeelee@uchicago.edu.
† E-mail: jkurutz@uchicago.edu.

[1] Abbreviations: SP-A, SP-B, SP-C, SP-D, surfactant protein A, B, C, and D, respectively; LS, lung surfactant; NRDS, neonatal respiratory distress syndrome; CD, circular dichroism; FTIR, Fourier transform infrared spectroscopy; NMR, nuclear magnetic resonance; NOE, nuclear Overhauser effect; NOESY, NOE spectroscopy; DQCOSY, double quantum filtered correlation spectroscopy; TOCSY, total correlation spectroscopy; DSS, 3-(trimethylsilyl)propane-1,1,2,2,3,3,-d_6-sulfonic acid, sodium salt; FID, free induction decay; WET, water suppression enhanced through T_1 effects; MRE, mean residue ellipticity; RMSD, root-mean-squared deviation; CSI, chemical shift index; CVFF, constant force field; PDB, protein data bank.

10.1021/bi016077x CCC: $22.00
Published on Web 07/02/2002

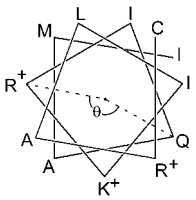

FIGURE 1: Helical wheel representation of putative helical region in SP-B_{11-25}. θ is the "polar angle," which is the angle subtended between polar residues in an amphiphilic α helix, as defined by Uematsu and Matsuzaki (*40*). Here, the polar angle is approximately 160°, which is purported to promote association of the peptide with the lipid films without forming pores.

is proposed to be important for anchoring SP-B in the lipid monolayer (*32*, *33*). The truncated peptide SP-B_{11-25}, which lacks this tail, does not reduce the surface tension of mixed phospholipid monolayers as efficiently as SP-B_{1-25} (*33*). The two peptides also exhibit different effects on monolayer 2D phase morphology (*33*). Yet Langmuir surface pressure−area isotherms clearly indicate that SP-B_{11-25} associates with the monolayer (*33*). Thus, SP-B_{11-25} is the focus of our study here.

The general structure of SP-B and its derivatives has been investigated with both theoretical and experimental tools. Secondary structure prediction algorithms, including the hierarchical neural network method of Guermeur (*34*, *35*) and the Jpred consensus method (*36*, *37*), which surveys results from multiple structure prediction methods, suggest that SP-B_{1-25} should be α-helical between residues 11 and 22, leaving the remaining N- and C-terminal residues relatively unstructured. These predictions have been confirmed in structural studies that used circular dichroism (CD) and Fourier transform infrared spectroscopy (FTIR) to direct molecular modeling of SP-B_{1-25} (*38*, *39*). Threading the sequence into a helical wheel representation (Figure 1) suggests that the proposed helix is amphiphilic with a polar angle (the angle subtended between the two outermost polar residues in the wheel) of approximately 160°, which may help explain its surface activity and biochemical function (*40*). With this foundation, we sought to provide additional information on SP-B structures using nuclear magnetic resonance (NMR) techniques.

To help correlate SP-B function with structure, we determined the predominant conformations of the SP-B_{11-25} peptide in methanol solution using NMR spectroscopy combined with restrained simulated annealing molecular modeling. Methanol is a popular mimic of the lipid environment, having been used as the solvent or a major solvent component in the NMR structure determinations of many membrane peptides, including SP-C (*41*), melittin (*42*, *43*), zervamicin (*44*), and other peptides and peptide analogues (*45*−*47*). Its use affords solubility of the peptide and stabilizes helical structure (*48*). Using methanol solutions of the peptide also provides a basis against which future work performed with aqueous micelle suspensions can be compared (e.g., *49*, *50*): if the methanolic structure is different from that in a micelle, one can conclude that the restrictive environment on the micelle plays a role in determining peptide structure. Preliminary nuclear Overhauser effect spectroscopy (NOESY) (*51*−*54*) experiments were acquired at room temperature to identify hydrogen pairs that are close in space, but they revealed few significant NOE cross-peaks. Previous NOESY experiments on SP-B_{11-25} conducted by Kumar and Wiedmann, on which our studies build, were performed at 40 °C and revealed even fewer NOESY cross-peaks (*32*). Kumar and Wiedmann, however, obtained CD and non-NOE NMR data, such as $^3J_{H^NH^\alpha}$ and amide ^{1}H exchange rates, that suggested partial helical structure in the absence of confirmatory NOESY cross-peaks. To stabilize the peptide's structure and enhance NOESY cross-peak volumes by slowing the molecular tumbling rate (*53*), we performed our experiments at 5 °C. Structural data were used to guide a series of molecular modeling experiments that would yield a good set of coordinates for the peptide. A family of acceptable energy-minimized structures was identified, and then selected members of the family were subjected to 0.95 ns of molecular dynamics simulation at 1000 K to assess agreement between static and dynamic molecular descriptors.

We found general agreement with theoretical predictions that SP-B_{11-25} is primarily helical. In our models, Φ and Ψ angles from residues L14 to M21 agree closely with those of the canonical α-helix. The helix is slightly frayed at the N-terminus, and P23 breaks the helix at its C-terminus. Little NOE data were obtained for terminal residues C11, R12, K24, and G25, probably due to conformational flexibility.

MATERIALS AND METHODS

Materials and Equipment. The SP-B_{11-25} peptide was obtained as a 95% pure powder from SynPep. Both NMR and CD experiments used 1.25 mM peptide dissolved in CD_3-OH (98% D, Isotec) with 0.1 mM DSS-d_6 (3-(trimethylsilyl)-propane-1,1,2,2,3,3,-d_6-sulfonic acid, sodium salt, Cambridge Isotope Labs) as a chemical shift reference (*55*). The apparent pH was approximately 6.0. CD spectra were obtained on an Aviv model 215 CD spectrophotometer equipped with a thermoelectric temperature controller. The CD sample cell (Hellma) had a path length of 0.01 cm, enabling CD of the peptide to be acquired at concentrations appropriate for NMR samples. NMR spectra were recorded on a Varian Inova 600 MHz spectrometer equipped with *z*-axis gradients and an RF waveform generator in the University of Chicago Biological Sciences Division NMR facility. NMR spectra were analyzed using Varian's VNMR software.

NMR Data Acquisition and Processing. Standard 2D NMR spectra were obtained for assignment and distance measurement. Scalar-coupled spin systems were identified using double quantum filtered correlation spectroscopy (DQCOSY) (*54*, *56*) and total correlation spectroscopy (TOCSY) (*54*, *57*). The DQCOSY comprised 512 t_1 scans of 4096 t_2 points, acquiring 32 FID's per scan, and employed a 0.75 s interscan delay. The TOCSY spectra used 450 t_1 scans of 4096 t_2 points, acquiring 32 FID's per scan, and used a 1.0 s interscan delay. We collected two TOCSY spectra, with mixing times of 15 and 50 ms. Our TOCSY experiments featured DIPSI-2 spin-locks to achieve uniform coherence transfer across the spectrum (*58*, *59*). NOESY spectra (*51*−*54*) with 250 ms mixing times were acquired for ^{1}H−^{1}H distance measurements. The NOESY spectra used 450 t_1 scans of 4096 t_2 points, acquiring 32 FID's per scan, and used a 1.5 s interscan delay. WET solvent suppression (*60*) was used in all NMR experiments, and for the NOESY spectrum, the WET sequence element was placed in the mixing time, not in the

interscan delay. NOESY spectra were processed using VNMR software, zero-filled to 8192 × 2048 points, and weighted with a 90°-shifted sine-bell window with small additional Gaussian window components (VNMR coefficients: 0.285 (t_2) and 0.062 (t_1)) prior to Fourier transformation. Baselines were corrected using the spline fitting routine in VNMR, and manually defined cross-peaks from the baseline-corrected NOESY spectrum were integrated using VNMR routines.

Computational Modeling. Molecular modeling was accomplished using the program suite InsightII and its modules Discover and DeCipher (Molecular Simulations, Inc./Accelrys). Insight's constant valence force field, CVFF, was employed in all simulations (*61*, *62*). Simulated annealing was performed on three different starting structures: extended strand ($\Phi = 0°$, $\Psi = 0°$), canonical β-sheet ($\Phi = -120°$, $\Psi = +120°$), and canonical α-helix ($\Phi = -60°$, $\Psi = -40°$). Each round of annealing consisted of 5.0 ps of initial conjugate gradient energy minimization (time step = 1.0 fsec; timtmp, the exponential decay constant describing coupling to the temperature bath = 0.02 ps), then 26 cycles comprising 1.0 ps of quick heating to 1000 K (timtmp = 0.3), 20.0 ps of dynamics at 1000 K (timtmp = 0.02), 50.0 ps of cooling to 20 K, and 5.0 ps of energy minimization.

Restraints were established for $^1H-^1H$ distances and dihedral angles, and force constants were kept relatively weak with the expectation that this short peptide would be flexible and the long mixing time employed in the NOESY spectrum might lead to underestimation of $^1H-^1H$ distances. Dihedral restraints, invoked on the basis of the $^1H^\alpha$ chemical shift index (CSI) and prior FTIR data (*38*, *39*), consisted of potential energy wells with no penalty between $\Phi = -70°$ to $-50°$ and $\Psi = -55°$ to $-35°$, with harmonic force constants of 50 kcal/(mol rad^2) outside those limits. Thus, 1.0 kcal/mol penalties were incurred for 8.1° deviations outside the boundaries. NOE cross-peak volumes were calibrated against cross-peak volumes between well-separated geminal $^1H^\beta-^1H^\beta$ signals, classified as strong, medium, and weak and translated into distance restraint upper bounds of 3.2, 4.0, and 5.0 Å. Lower bounds were all set to 1.7 Å. NOE contacts to one or both ^{1}H's within a CH_2 group were manifested as restraints to pseudoatoms until, when appropriate, further refinement enabled assignment of the ^{1}H signals to their prochiral atoms. To allow for the difference in position between pseudoatoms and hydrogens, we added 0.5 Å to the upper bounds of each pseudoatom restraint. Force constants for distance restraints were 10 kcal/(mol Å^2), so 1.0 kcal/mol penalties were incurred for distance violations of 0.32 Å.

Simulated annealing proceeded in multiple rounds, each with progressively larger sets of distance restraints. Three sets of annealing, corresponding to the three different starting structures, were performed in parallel. The first round of annealing employed α-helical dihedral restraints on the Φ and Ψ angles of A13 through M21 and distance restraints only between backbone ^{1}H's. The second round of simulated annealing used the final structures from each of the three first rounds and added distance restraints between backbone and side chain ^{1}H pairs. Iterative refinement of the restraint set was accomplished by evaluation of restraint violations at the end of each annealing stage, rectifying assignment of overlapped peaks, and determining chiral restraints, followed by re-execution of simulated annealing and evaluation of potential resolution of restraint violations. Distances and dihedral angles from families of minimized structures were measured using the Analyze and DeCipher tools within InsightII and were exported for analysis in Excel (Microsoft). After all annealing had been performed, all structures within 5.0 kcal/mol of the lowest-energy structure were collected from all three refined annealing runs to represent the family of most probable low-energy structures. Coordinates for this 17-member family have been deposited, with restraints and NMR data, at the Protein Data Bank (PDB) under the code 1KMR.

Molecular Dynamics. Because no family of minimized structures can completely describe the solution conformation of any molecule, restrained molecular dynamics was performed on SP-B_{11-25}. All NOE data represent time-averaged distances between nuclei within flexible molecules whose instantaneous conformation may differ significantly from the structure with minimum energy. Restrained dynamics was performed at 1000 K for 1.25 ns for each starting structure. The elevated temperature was employed to ensure satisfactory sampling of alternative conformations over this limited time scale. 1900 structures in the final 0.95 ns of the dynamics trajectory were sampled at regular intervals for analysis. $^1H-^1H$ distances were averaged as $\langle r_{\text{instantaneous}}{}^{-6}\rangle^{-1/6}$ to reflect the NOE signal expected to be observed from such a population. Backbone Φ and Ψ angles were also sampled and averaged for comparison to their values in the minimized structures.

RESULTS AND DISCUSSION

Circular Dichroism. The overall structure of the SP-B_{11-25} peptide in methanol (1.25 mM peptide in CD_3OH with 0.1 mM DSS-d_6) was assessed by CD. Data in Figure 2 are presented here as mean residue ellipticities (MREs), which can quantitatively indicate the degree of peptide helicity. Data were taken at different temperatures, 5°, 25 °, and 45 °C, to ascertain the peptide's thermal stability and estimate how much structure is exhibited at different temperatures, which may shed light on the previous structure determinations performed at different temperatures. MRE values at 222, $[\theta]_{222}$, indicate that 29% of the peptide is helical at 45 °C, 35% at 25 °C, and 43% at 5 °C, according to the method of Chen, which was derived for aqueous polypeptide solutions (*63*). According to the method of Jibson and Li,(*48*) which was calibrated for CD measurements in 90% aqueous methanol solutions, $[\theta]_{221}$ suggests that SP-B_{11-25} is 27%, 35%, and 44% helical at these temperatures, respectively. Assuming that only the region from L14 to M21 is capable of contributing helical character, the central portion of the peptide is thus approximately 53%, 65%, and 82% helical at these temperatures, probably reflecting a degree of dynamic instability that reduces the time-averaged CD signal relative to a perfect rigid helix. Interestingly, these CD spectra exhibit an isodichroic point, indicating that the molecule partakes of a two-state equilibrium, presumably between helix and random coil. The exact location of the isodichroic point, 199 nm, was found by taking the average of the magnitudes of all possible differences between MRE values at every wavelength (λ):

$$\text{Average}(|[\theta]_\lambda(45°) - [\theta]_\lambda(25°)|, \quad |[\theta]_\lambda(45°) - [\theta]_\lambda(5°)|, \quad |[\theta]_\lambda(25°) - [\theta]_\lambda(5°)|)$$

The plot of this function versus wavelength (Figure 2B) yielded a conspicuous minimum at 199 nm indicating the wavelength of the isodichroic point.

NMR Data. NMR Spectra were acquired at 5 °C, and resonance assignments were made with standard methods (*64*). Scalar-coupled spin systems were identified in DQ-COSY and TOCSY experiments, and sequential assignments were made using backbone H^N-H^N and H^N-H^α NOESY cross-peaks. Sequential connectivity in the H^N-H^N and H^N-H^α regions of the NOESY spectrum is shown in Figure 3. Assignment was assisted by the preliminary NMR analysis of SP-B_{11-25} by Sandeep Kumar (*32*). Sequential NOE contacts are identified in Figure 3. Assignments of the ^1H resonances and values for $^3J_{H^NH^\alpha}$ scalar coupling constants, determined using NOESY and DQCOSY spectra when measurement was not possible in 1D spectra, are given in Table 1. Scalar couplings too small to measure accurately were reckoned to be less than 5.0 Hz. Classifications of $^3J_{H^NH^\alpha}$ values as <5.0, >8.0, and between 5.0 and 8.0 Hz are shown in Figure 4.

Assignments were made for all observable signals in the SP-B_{11-25} spectra (Table 1). Some peaks were partially overlapped, and though resonances could be assigned unequivocally, such overlap made some NOE cross-peaks unsuitable for use as restraints. For instance, the amide resonances for R17 and I18 are just 0.02 ppm apart, making it impossible to detect sequential $H^N(17)-H^N(18)$ and $H^\alpha(17)-H^N(18)$ NOE cross-peaks. For some residues around residue M21, a second set of resonances was observed exhibiting identical patterns of NOE connectivity to the primary set (Figure 3). We ascribe this duplication to methionine oxidation, as was observed in the NMR analysis of SP-C (*41*). In another study being conducted by our lab, NMR data from a methionine-to-norleucine analogue of SP-B_{11-25}, in which the sulfur atom is replaced with a methylene group, exhibit a single set of peaks almost identical to the predominant set treated here, supporting the hypothesis that methionine oxidation gives rise to the duplication. Cross-peaks to H^N resonances of C11 and R12 were faint when observed and exhibited significant NOESY cross-peaks at the solvent frequency, suggesting they undergo appreciable exchange with solvent. The H^N chemical shift of residue R12 was uncharacteristically downfield (9.34 ppm), though weak DQCOSY, TOCSY, and NOESY cross-peaks confirm its identity. Stereospecific assignments were made by analyzing annealed structures that had been restrained using pseudoatoms and assigning hydrogen identities on the basis of the plausibility of the possible assigned NOE patterns. In cases where NOEs were insufficient to distinguish between opposite assignments, stereospecific assignments were not made, and restraints were made to pseudoatoms. Restraint violations for chiral hydrogens were closely monitored, and when many violations appeared, the effects of switching assignment were tested by repeating the annealing routine with restraints of opposite chirality.

Qualitative Structure Indicators. Preliminary structural characterization was accomplished by examining several qualitative structure indicators, including $^3J_{H^NH^\alpha}$ coupling constants, NOE contact patterns, and the H^α chemical shift index (Figure 4). The most significant pattern observed here is the set of NOE's between H^α signals on residues i and H^N of residues $i + 3$, which indicates α helical structure (*65*). SP-B_{11-25} exhibits such contacts from residues R12 through I22, as highlighted by arrows in Figure 3. Other contacts supporting helical structure include $H^\alpha \rightarrow H^\beta(i+3)$ NOE's, which were also observed from residues R12 through I22. For each residue's H^α resonance, we calculated its CSI, which bears the value of -1 if its frequency is 0.1 ppm less than the chemical shift (upfield) for that residue's signal if it were in an unstructured pentapeptide, $+1$ if it is 0.1 ppm greater than the random coil value (downfield), and 0 if it is within 0.1 ppm (*66*, *67*). A group of residues exhibiting CSI $= -1$ suggests an α helix, and a group where CSI $= +1$ indicates a β sheet. Though the CSI technique was originally developed for aqueous samples, Merutka et al. have reported the chemical shift dependence on trifluoroethanol concentration for H^α chemical shifts and found that they were not changed significantly from their aqueous values, the largest deviation being merely 0.04 ppm (*67*). However, these authors also found that H^N chemical shifts are significantly different in alcohol solutions, so we deliberately did not use H^N signals in our CSI analysis. We have conducted some preliminary experiments comparing methanolic chemical shifts of amino acids and some pentapeptides and have found no H^α chemical shifts differences from reference (aqueous) values greater than 0.03 ppm. Thus, the patterns of NOE contacts and the CSI values indicate that SP-B_{11-25} is likely to be helical between residues A13 and M21, though the $^3J_{H^NH^\alpha}$ value of M21 suggests that the helix ends at A20.

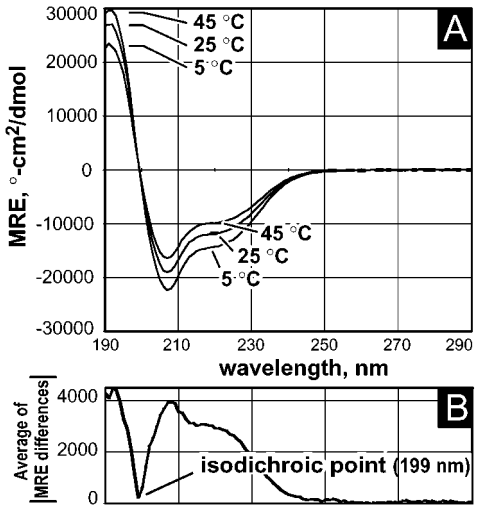

FIGURE 2: (A) Circular dichroism spectra of 1.25 mM SP-B_{11-25} dissolved in CD_3OH solution with 0.1 mM DSS, taken at 5, 25, and 45 °C. Mean residue ellipticity (MRE) values at 221 nm indicate that the peptide is approximately 44% helical under the same conditions as the NMR experiments (5 °C), according to the methanol-calibrated algorithm of Jibson and Li (*48*). This percentage is reduced to 35% at 25 °C and 27% and 45 °C, indicating that helix stability is enhanced at lower temperatures. The results at 5 °C are consistent with approximately 82% helical content between residues L14 and M21, assuming that all the helix component is found in that region. (B) Average of the differences between spectra (see text for equation). The minimum, observed at 199 nm, indicates an isodichroic point, which suggests that the peptide partakes of a two-state equilibrium, presumably between helix and random coil.

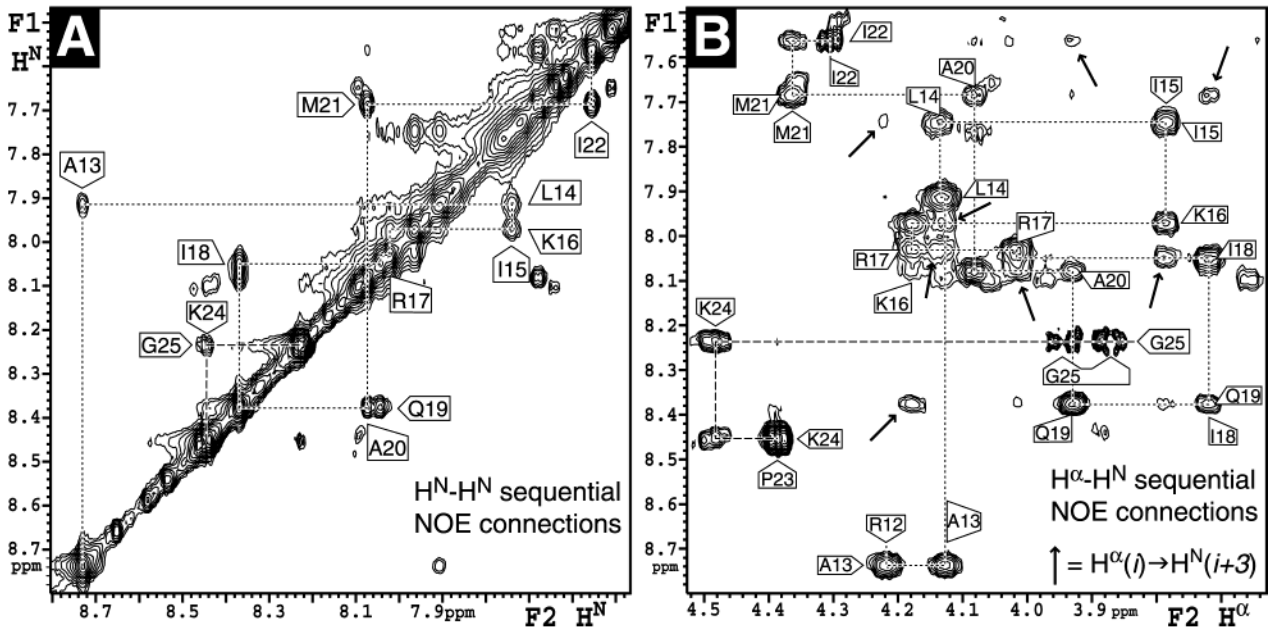

FIGURE 3: Portions of the NOESY spectrum of 1.25 mM SP-B_{11-25} in CD_3OH, acquired at 5 °C using a 250 ms mixing time and WET solvent suppression during the mixing period. Chemical shifts are referenced to internal 0.1 mM DSS. Using 32 scans per point, 4096 t_2 and 450 t_1 points were acquired for this spectrum with an interscan delay of 1.5 s, then weighted by 90°-shifted sine-bell windows with a small extra Gaussian component (VNMR parameters for the Gaussian are 0.285 (t_2) and 0.062 (t_1)), and zero-filled to 8192 × 2048 points. Sequential connections are indicated by dashed lines and flags. Unlabeled peaks of appreciable intensity correspond to a duplicate set brought about by partial methionine oxidation. (A) The H^N-H^N region of the NOESY spectrum, with sequential $H^N(i)-H^N(i+1)$ cross-peaks highlighted with dashed lines. Many potential $H^N(i)-H^N(i+2)$ cross-peaks are obscured by spectral overlap, and others are faint, but present, though they do not necessarily appear in the plot at this vertical scale. (B) The region of the same NOESY spectrum showing $H^\alpha-H^N$ NOE contacts. Sequential contacts are indicated by dashed lines and flags. Important helix-indicating $H^\alpha(i) \rightarrow H^N(i+3)$ cross-peaks are indicated with arrows. Several peaks of appreciable intensity at the top of this plot duplicate patterns in the labeled section, suggesting that they indicate partial oxidation of residue M21, as observed by Johansson for SP-C (*41*).

Table 1: ^1H Chemical Shift Assignments (ppm) and $^3J_{H^NH^\alpha}$ (Hz) Values for SP-B_{11-25} in CD_3OH at 5 °C

residue	H^N	H^α	H^β	H_{other}	$^3J_{H^NH^\alpha}$
C11	8.41	4.43	3.24, 3.69	–	ND
R12	9.34	4.22	1.80, 1.91	γ 1.69, δ 3.22, ϵ 7.71, $\eta(Z)$ 6.91, $\eta(E)$ 7.36	ND
A13	8.71	4.13	1.45	–	<5.0
L14	7.90	4.14	R_p 1.69, S_p 1.76	γ 1.68, δ 0.935, δ 0.995	<5.0
I15	7.74	3.79	1.99	$\gamma(R_p)$ 1.28, $\gamma(S_p)$ 1.63, γ(Me) 0.925, δ 0.885	<5.0
K16	7.96	4.18	R_p 1.91, S_p 1.86	γ 1.57, δ 1.69, ϵ 2.88,2.94, ζ 7.87	<5.0
R17	8.02	4.02	R_p 1.98, S_p 1.80	γ 1.64, δ 3.17, ϵ 7.51, $\eta(Z)$ 6.78, $\eta(E)$ 7.33	<5.0
I18	8.04	3.73	1.98	$\gamma(R_p)$ 1.105, $\gamma(S_p)$ 1.80, γ(Me) 0.90 δ 0.84	5.0
Q19	8.36	3.93	R_p 2.28, S_p 2.01	$\gamma(R_p)$ 2.28, $\gamma(S_p)$2.60, $\epsilon_{22}(Z)$ 6.93, ϵ_{21} (E) 7.64	<5.0
A20	8.07	4.08	1.51	–	<5.0
M21	7.68	4.37	R_p 2.19, S_p 2.16	$\gamma(S_p)$ 2.59, $\gamma(R_p)$ 2.77, ϵ 2.05	6.7
I22	7.55	4.30	1.90	$\gamma(R_p)$ 1.24, $\gamma(S_p)$ 1.83, γ(Me) 1.00, δ 0.885	5.7
*P*23	–	4.385	R_p 1.95, S_p 2.27	$\gamma(S_p)$ 1.96, $\gamma(R_p)$ 2.10, $\delta(R_p)$ 4.03, $\delta(S_p)$ 3.65	–
K24	8.43	4.49	1.97, 1.72	γ 1.57, δ 1.65, ϵ 2.89, ζ 7.76	8.6
G25	8.21	3.96, 3.86	–	–	5.3

Restrained Simulated Annealing. NMR and previously published FTIR data were translated into distance and dihedral angle restraints for use in molecular modeling. NOESY cross-peaks were integrated, and corresponding upper-bounds distance restraints were assigned as described in the Methods section. After refinement of the data, these included 131 interresidue distance restraints and 144 intraresidue distance restraints, resulting in an average of over 18 distance restraints per residue. Helical backbone dihedral angle restraints were imposed from residues A13 through I22 on the basis of the chemical shift index data and the FTIR data for SP-B_{1-25} reported by Gordon et al. (*38*). These authors assigned helical character to residues C8 through I22 on the basis of IR $^{13}C{=}O$ stretch frequencies acquired for over 70% of the residues in the peptide SP-B_{1-25}. Their data was used to construct the SP-B_{1-25} model 1DFW in the PDB (*39*, *68*). These observations also indicated hydrogen bonding in the helix, so for our work we included restraints on the 6 backbone $CO(i)\cdots H^N(i+4)$ hydrogen bonds A13···R17 through I18···I22. The force constants applied to distances and dihedral angles were 10 kcal/(mol Å^2) and 50 kcal mol^{-1} rad^{-2}, which impose 1.0 kcal/mol penalties for incursions of 0.32 Å and 8.2°, respectively. These restraints were approximately half as strong as those applied to SP-C in its methanol solution structure determination (*41*, *69*) and one-fifth as strong as those used in the 1DFW SP-B_{1-25} model (*39*, *70*), which allowed our models a greater degree of flexibility and ensured more realistic dynamics behavior.

Annealing was performed using the routines described in the Methods section, and a family of accepted structures was

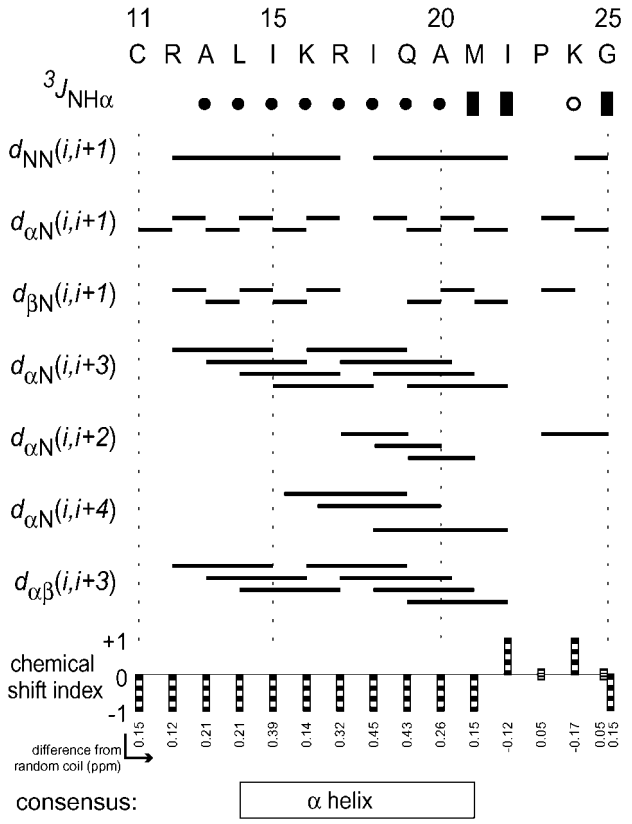

FIGURE 4: Qualitative structure indicators in SP-B_{11-25}, including selected NOE contacts, $^3J_{H^NH^\alpha}$ coupling constants, and chemical shift indices. Closed dots represent *J* values less than 5.0 Hz, open circles represent *J* values above 8.0 Hz, and vertical lines represent values between 5.0 and 8.0. $^3J_{H^NH^\alpha}$ values less than 5.0 Hz generally indicate Φ angles consistent with α helices. The pattern of $H^\alpha(i) \rightarrow H^N(i+3)$ and $H^\alpha(i) \rightarrow H^\beta(i+3)$ contacts indicates α-helical structure. Some sequential NOEs could not be identified conclusively because of peak overlap. The CSI's for the H^α resonances were calculated according to the method of Wishart et al. (*66*), using the random coil chemical shifts of Merutka et al. for aqueous pentapeptides H−GGXGG−OH at 5 °C (*67*). In this method, regions where CSI predominantly equals −1 are probably α helical, and regions where CSI is mostly +1 are probably *β* sheet. Actual differences, in ppm, between H^α chemical shifts in the peptide and their random coil values are reported underneath each CSI column. Note that Merutka et al. reported that the chemical shifts of H^α resonances, unlike those of H^N, did not change significantly with trifluoroethanol concentration, supporting the validity of using them to interpret our methanolic data. Moreover, our comparisons of some test peptides and amino acids dissolved in neat methanol showed no significant differences in chemical shift from the aqueous solutions.

derived. Each of the three parallel annealing runs yielded 26 energy-minimized structures. The one with the lowest energy was identified, and all others with energies less than 5.0 kcal/mol of that structure's energy were included in the family of accepted structures. This procedure resulted in 17 structures, shown superimposed on one another in Figure 5. Of the 4624 distance restraints imposed on the family, 192 were violated by more than 0.32 Å (1.0 kcal/mol). Of the 340 dihedral angle restraints placed on the family, 16 were violated by more than 8.1° (1.0 kcal/mol), two of which correspond to the Ψ angle of residue A13 and 14 of which correspond to the Ψ angle of residue I22. When the structures are aligned to minimize the root-mean-squared standard deviation (RMSD) for backbone heavy atoms from residues A13 through M21, the average backbone heavy atom RMSD

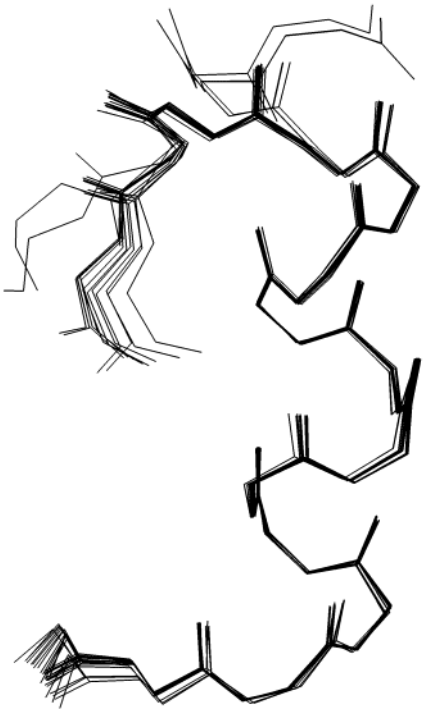

FIGURE 5: Backbone traces of the 17 lowest-energy annealed structures for SP-B_{11-25}. Structures were aligned to minimize heavy-atom differences between residues I14 through M21 and the corresponding atoms of the lowest-energy structure. The two C-terminal residues exist in three distinct conformations, and the N-terminus exhibits some fraying. The coordinates for these models are found under the PDB entry 1KMR.

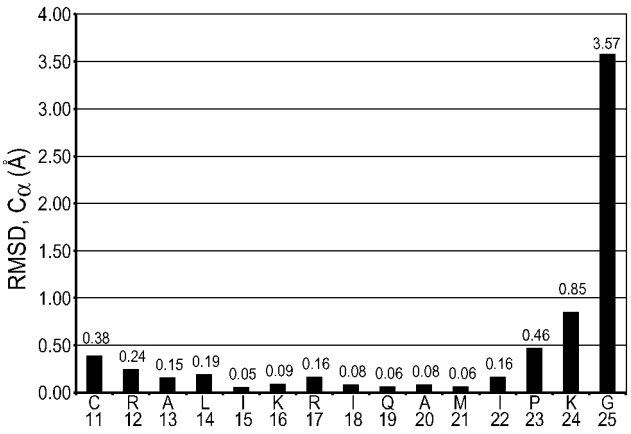

FIGURE 6: RMSD's of backbone heavy atoms in each of the structures from the average structure when the family of structures is aligned as shown in Figure 5. Clearly, the family is highly structurally homologous in the helical region and is frayed at the termini. The multiple conformations available to the two residues at the C-terminus increases the RMSD values significantly.

is 0.96 ± 2.45 Å, and the average backbone atom RMSD for residues L14 through M21 is 0.09 ± 0.12 Å. The discrepancy between these two numbers reflects the fraying of the termini that is included in the first RMSD value. The disorder at the termini is clearly reflected in the plot of backbone heavy-atom RMSD versus residue, shown in Figure 6. The large standard deviation for the whole peptide RMSD reflects large conformational variability at the C-terminus, which is discussed below.

Dependence of the annealed structures on their initial conformations was assessed. Each of the three starting conformations gave rise to several annealed structures in the

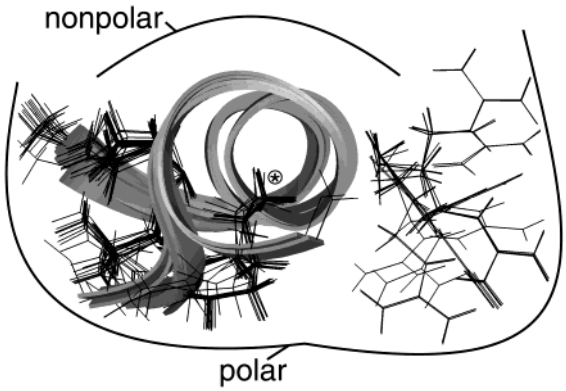

FIGURE 7: Distribution of polar side chains about the helix axis, as seen from its C-terminal end. All 17 family members are superimposed, and only the polar side chains K16, R17, Q19, and K24 are shown in atomic detail. The polar side chains of the helix are grouped in the bottom portion of the helix, thus establishing its amphiphilicity. The R17 side chain at the right is more disordered than the others and distant from the other cationic groups, presumably to relieve Coulombic repulsion arising primarily from K16. Note the placement of the K24 amine group, marked with an asterisk (*), at the C-terminus of the helix in most of the structures. This position helps stabilize the helix dipole.

final representative family. Four of the final 17 started as extended strand, five started as canonical α helix, and eight came from canonical β sheet. If any dependence of the annealed structures on their initial conformations were to appear, one would expect that the final, predominantly α helical, set would be biased in favor of the α helix starting structure, but this is not the case here (*71*). Moreover, all three starting structures were represented across the 5 kcal/mol energy spectrum, indicating there was no predetermined energy hierarchy imposed by the starting conformations. Thus, we conclude our method adequately sampled the relevant conformational space and our minimized structures probably represent the major minima in this peptide's energy landscape.

Helix Boundaries. Formal determination of helix boundaries took into account many factors. CSI indicates helix from residue A13 through M21. Helical signature NOE's $H^{\alpha}(i) \rightarrow H^{N}(i+3)$ suggest a helix from R12 through I22. Analysis of the family by the program PROCHECK(*72*) on the PDB's ADIT validation server indicates helical character from A13 through M21. But the annealed structures exhibit some dihedral restraint violations at Ψ(A13) and Ψ(I22), suggesting that these might not be best described as helical. Interpreting our data conservatively, we ascribe α helical character to residues L14 through M21.

Amphiphilicity. Examining the distribution of charged side chains about the helix axis is a good way of assessing the degree to which SP-B_{11-25} is amphiphilic. As shown in Figure 7, which displays only the backbone and the polar side chains of the helix, there is a cluster of polar side chains on one side of the helix when viewed on end. (In this figure, all 17 structures in the family are displayed simultaneously.) The K24 side chain amine caps the helix and is marked with an asterisk in Figure 7. The C-terminus and the side chains of K16 and Q19 are clustered on the lower left portion of the helix, and R17 appears on the opposite side. The separation of K16 and R17 side chains is consistent with Coulombic repulsion between their like charges. This distribution of polar side chains clearly leaves a gap, shown here as an absence of side chains at the top of the helix, that is filled with nonpolar side chains. The α helix of SP-B_{11-25} can thus be divided into two roughly equal sections, one polar and one nonpolar, suggesting that this helix is amphiphilic. We note, however, that the polar angle (*40*), defined by the angle subtended between the Q19 and R17 side chains, adopts many diverse values because of the variability in R17 side chain position. Because of side chain flexibility, precise structural measures of amphiphilicity such as the polar angle are unlikely to correlate strictly with surface activity. Thus, we restrict our conclusion to simply finding that the SP-B_{11-25} helix is amphiphilic and refrain from further discussion concerning the quantitative implications of this structural parameter.

Dynamics Behavior. Restrained molecular dynamics simulations of SP-B_{11-25} were conducted to determine whether the annealed structures adequately represented the peptide in solution. Starting structures for each of the three dynamics simulations were the lowest-energy annealed structures from each of the three annealing runs. Minimized structures were brought to 1000 K, allowed to equilibrate for 150 ps, and permitted to move about for 950 ps. The nonphysiological temperature was chosen to stringently challenge the annealed structures, giving them sufficient energy to leave local conformational energy minima if they had been unduly trapped by incompatible restraints. With this in mind, the same force constants used in the annealing runs were also used in the dynamics runs, though other researchers sometimes increase the force constants as the temperature increases (*39*, *70*).

Analysis of the Φ and Ψ angles of the peptide during the molecular dynamics simulations provides a more detailed picture of the molecule's secondary structure. It is particularly useful to compare these results with those obtained from the family of accepted annealed structures, as is shown in Figure 8. The dynamics data (open columns, Figure 8) show that SP-B_{11-25} adopts helical backbone dihedral angles from approximately residue L14 through M21 and exhibits strained helical values at residues A13 and I22. There is generally good agreement between the structures from dynamics simulations and the annealed structures (open columns, Figure 8). One exception to this result is the lack of any structures with $\Phi_{K24} \sim -120°$ in the dynamics trajectories while the family of 17 annealed structures includes three such structures, which have the highest energies of the peptide family. Thus, the conformations of the C-terminal two residues described by these three annealed structures may not be relevant to the peptide's solution behavior. The dynamics simulations also indicate Ψ_{K24} exhibits two broad roughly equally populated conformations centered around $-70°$ and $+60°$, whereas only one annealed structure is found with $\Psi = -71°$. This probably indicates small differences in energy between local minima, observable in the low-energy structures, that are not significant at higher temperatures. The static low-energy structures indicate that the peptide termini are somewhat frayed, but the wide range of backbone dihedral angles adopted by R12, P23, and K24 during the dynamics simulations make this variability abundantly clear. Thus, we observe good agreement between annealed and dynamic structures in the helical region from A13 through I22, and we observe less agreement and more disorder at the peptide termini.

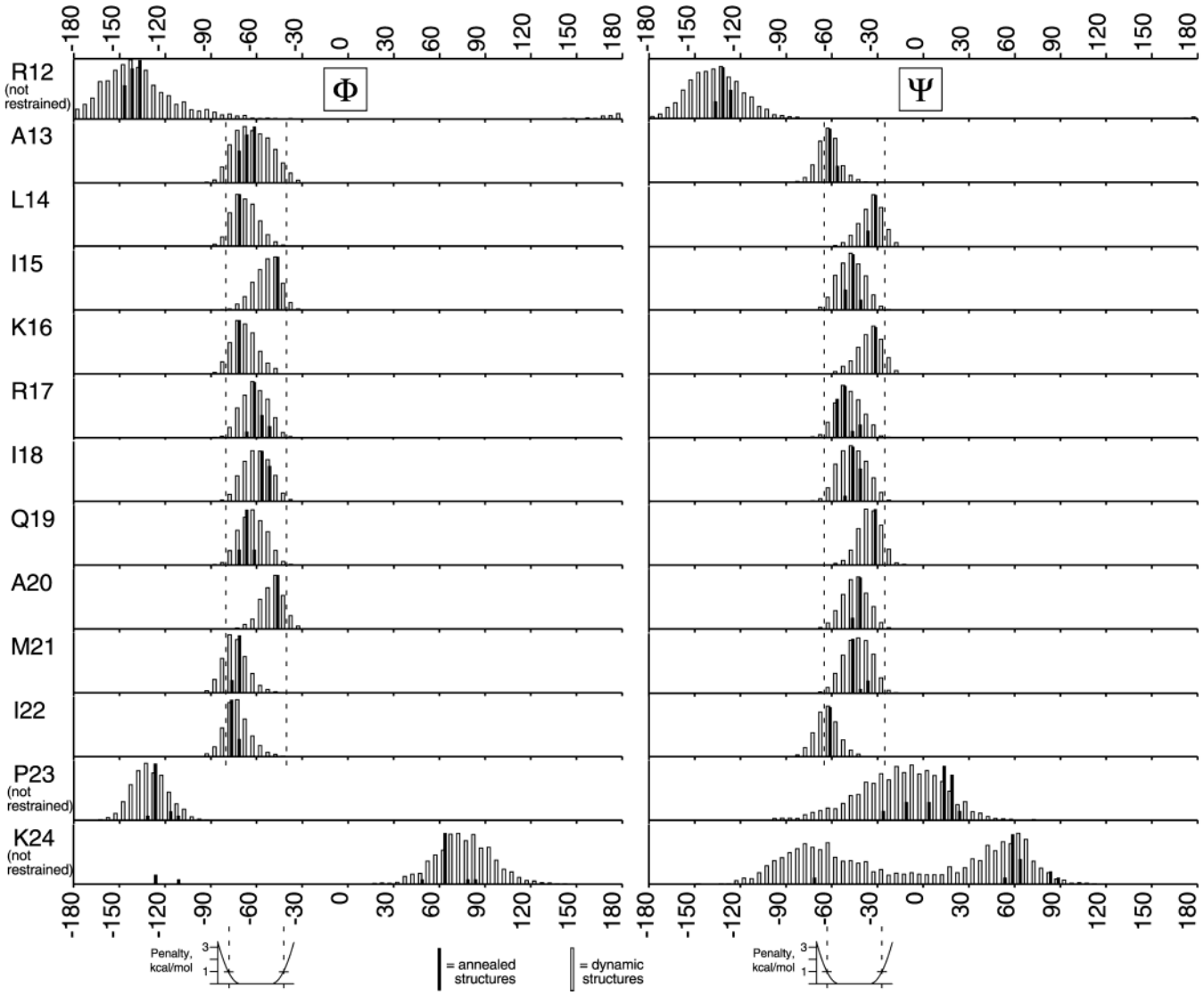

FIGURE 8: Φ and Ψ angles adopted by SP-B_{11-25} in the family of 17 annealed structures (closed columns) and during one of the three 950 ps restrained molecular dynamics simulations at 1000 K (open columns). Each bar represents the number of structures in which the examined dihedral adopts a value within a specified 5° range. Vertical scales for each angle histogram vary so the tallest peaks will occupy approximately the full vertical range of the plot. The dashed vertical lines represent the dihedral angles at which 1.0 kcal/mol penalties are imposed by the restraints, rounded to the closest 5° increment outside the real 1.0 kcal/mol barrier. Note that backbone dihedral restraints were not imposed on residues R12, P23, and K24. The starting conformation for this dynamics simulation was the most stable in the final family of annealed structures. Our data show that SP-B_{11-25} generally adopts helical backbone dihedral angles from approximately residue L14 through M21, with A13 and I22 adopting strained helical conformations. There is generally good agreement between the structures from dynamics simulations and the annealed structures, but some discrepancies are observed at the terminal residues R12, P23, and K24. These differences primarily reflect fraying at the termini, which is more pronounced at high temperature.

Interproton distances measured in the annealed structures were compared to those in the high-temperature dynamics simulations to further assess the agreement between the two sets of models. Full details of restraints, average distances, and violations are provided in the Supporting Information. Thirty-three of the 281 measured distances in the dynamics simulations exhibited $\langle r^{-6}\rangle^{-1/6}$-averaged distances over 0.2 Å shorter than the corresponding averaged distance in the annealed structures. In contrast, only 9 of the 281 measured distances in the dynamics simulations had $\langle r^{-6}\rangle^{-1/6}$-averaged distances over 0.2 Å longer than the analogous averaged distance in the annealed structures, and the average of these nine deviations was just 0.26 Å. One would expect the higher temperature of the dynamics simulation to drive atoms farther apart, but instead the $\langle r^{-6}\rangle^{-1/6}$-averaged constrained distance shrank by 0.06 Å. This simply illustrates the greater weight given to shorter distances by the averaging method. On the basis of the similarity between averaged distances in the static and dynamic models, we conclude that the $^1H-^1H$ distances observed in the annealed structures reasonably reflect the NMR-observable average distances encountered in solution.

Comparison to Folds in Related Proteins. Our family of structures compares favorably with those derived for related proteins in the amoebapore superfamily, which contains the saposins, a well-studied protein family homologous to SP-B (*73*). The most significant homologous protein for SP-B in this regard is NK-lysin, the only saposin-like protein for which there is an NMR structure (PDB code 1NKL) (*74*). In the alignment of Liepinsh et al., which places cysteines in conserved positions, SP-B_{11-25} corresponds to NKL_{7-25} (NKL_{21-24} residues have no homologues in SP-B) (*74*). This

region of NK-lysin was determined by NMR to be an amphiphilic α helix, showing that, in this segment for which we now have data, the secondary structures of these molecules is similar, just as their primary structures are similar. Also, both SP-B_{11-25} and its NK-lysin homologue segment exhibit a polar angle (θ) of approximately 160° (Figure 1). Unlike SP-B_{11-25}, this segment of NK-lysin contains two anionic residues in addition to its three cationic side chains, giving rise to a +1 net charge. Saposin B does not have a PDB entry, but its structure has been investigated by CD, FTIR, and non-NOE NMR, and its segment bearing homology to SP-B_{11-25} has also been suggested to form an α helix with $\theta \sim 160°$, though with a −1 charge and no cationic residues (*75*). If Saposin C follows the trend suggested by homology, its analogous helical segment should be zwitterionic, containing two positive and two negative residues and should present a $\theta \sim 160°$ (*74*, *76*). The analogous region of the plant aspartic protease prophytepsin (residues 72−90), which bears a circularly permuted sequence homology with NK-lysin and Saposin C, has been shown to be α helical by X-ray crystallography (PDB code 1QDM) and is proposed to target the protein to Golgi membranes (*76*). Interestingly, the relevant prophytepsin helix has a net −1 charge, contains four uncharged polar residues, and, unlike any of the above protein segments, presents a polar angle of approximately 200°. Osanai et al. have shown that surfactant assembly follows a Golgi-independent secretion pathway (*77*), suggesting that the saposin/amoebaporin fold is important for membrane binding but that the charge and polar angle of the proteins' helices determine their affinity for specific lipid compositions. Thus, the helicity and polar angle of SP-B_{11-25} concur well with those of relevant segments in homologous proteins. It is striking, however, that SP-B_{11-25}, bearing a +3 charge in the helix, is the most positively charged in the family, the others bearing little or no net charge.

Functional Implications of SP-B_{11-25} Structure. The positive charge and its distribution about the SP-B_{11-25} helix may be relevant to SP-B function. Helical amphiphilicity in SP-B is important for its surface activity, but according to Jiapartinum, the 10-residue "insertion sequence" at the N-terminus is more important for retaining SP-B in the monolayer at high surface pressures (*33*). Also, the biological importance of SP-B is not so much that it reduces surface tension, but that it ensures that collapsed monolayers respread readily upon expansion. It appears to accomplish this by affecting the 2D phase behavior of the lipids at the air−water interface (*26*, *27*, *78*). Recent evidence suggests that SP-B may stabilize the coexistence disordered and ordered phases within the monolayer, which may promote the formation of "folded" membranes at high surface pressures that enable the rapid respreading of the protein−lipid film on the interface (*25*, *26*, *79*, *80*). Thus, the protein's function may be to help "stitch" the mutually repulsive anionic lipids together so they remain associated in the folds. In this case, a simple amphiphilic helix with a polar angle of 160° might optimally position cationic side chains for Coulombic interaction with widely spaced lipid headgroups. As such, the amphiphilic character of the helix would ensure that it lies roughly parallel with the interface plane, which would maximize the interaction of the peptide side chains with the lipid headgroups. This region of SP-B may be distinguished from other members of the amoebapore superfamily by its cationic nature, which is optimally designed to promote association with anionic lipid headgroups. The N-terminal 10 residues of SP-$B_{1-25\ and\ 1-78}$ may enhance the affinity of the peptide for the lipid monolayer and account for its surface activity, but the essential nature of SP-B may be its ability to tie many anionic lipid headgroups together so they do not break apart in the folding transition or become lost to the subphase upon monolayer collapse. The maximally spaced cationic side chains we observe in this NMR structure may be the key to SP-B function.

ACKNOWLEDGMENT

We are grateful to the American Lung Association, the March of Dimes, and the Searle Scholar Program/Chicago Community Trust for funding our research. We thank Dr. Alan Waring for helping design this project, for many useful discussions, and for bringing our attention to Sandeep Kumar's Master's Thesis. We thank Dr. Charles Fry of the University of Wisconsin−Madison for his practical instruction regarding the use of pulsed field gradients and the WET water suppression routine. We thank Dr. Robert Tappe of the University of Chicago for managing the Biological Sciences Division's NMR facility. We are grateful to Dr. Zbigniew Gasnya for maintaining the Chemistry Department's computational facilities. We also thank Professor Tobin Sosnick (U of C) for allowing us access to the new Biophysics Core Facility's circular dichroism spectrophotometer, and we thank Scott Walsh for help in keeping it running.

SUPPORTING INFORMATION AVAILABLE

(1) PDB-format coordinates (PDB code 1KMR), (2) chemical shifts in PDB format, (3) InsightII/Discover restraint file, (4) distance and restraint analysis of the final 17 structures, (5) distance and restraint analysis of structures from dynamics simultations, and (6) comparison of distances subject to restrain in annealed and dynamic structures. This material is available free of charge via the Internet at http://pubs.acs.org.

REFERENCES

1. Hawgood, S., Derrick, M., and Poulain, F. (1998) *Biochim. Biophys. Acta 1408*, 150−60.
2. Goerke, J. (1998) *Biochim. Biophys. Acta 1408*, 79−89.
3. von Neergaard, K. (1929) *Z. Gesamte Exp. Med. 66*, 373−394.
4. Clements, J. A. (1957) *Proc. Soc. Exptl. Biol. Med. 95*, 170−2.
5. Berne, R. M., and Levy, M. N. (1998) *Physiology*, 4th ed., Mosby Year-Books, St. Louis.
6. Avery, M. E., and Mead, J. (1959) *Am. J. Dis. Child. 97*, 517−523.
7. Collaborative European Multicenter Study Group (1988) *Pediatrics 82*, 683−91.
8. Robertson, B., and Halliday, H. L. (1998) *Biochim. Biophys. Acta 1408*, 346−61.
9. Suresh, G. K., and Soll, R. F. (2001) *Clin. Perinatol. 28*, 671−94.
10. Milligan, D. W., and Ainsworth, S. B. (2001) *Acta Paediatr. Suppl. 90*, 25−7.
11. Johansson, J., Curstedt, T., and Robertson, B. (1994) *Eur. Respir. J. 7*, 372−91.
12. Hall, S. B., Venkitaraman, A. R., Whitsett, J. A., Holm, B. A., and Notter, R. H. (1992) *Am. Rev. Respir. Dis. 145*, 24−30.
13. Pérez-Gil, J., and Keough, K. M. (1998) *Biochim. Biophys. Acta 1408*, 203−17.

14. Soll, R. F., and Blanco, F. (2001) in *Cochrane Database Syst. Rev.*, Cochrane Database Syst. Rev., Update Software, Oxford.
15. Johansson, J. (1997) *Biol. Neonate 71*, 49−52.
16. Walther, F. J., Gordon, L. M., Zasadzinski, J. A., Sherman, M. A., and Waring, A. J. (2000) *Mol. Genet. Metab. 71*, 342−51.
17. Johansson, J. (1998) *Biochim. Biophys. Acta 1408*, 161−72.
18. Hamvas, A., Cole, F. S., deMello, D. E., Moxley, M., Whitsett, J. A., Colten, H. R., and Nogee, L. M. (1994) *J. Pediatr. 125*, 356−61.
19. Tryka, A. F., Wert, S. E., Mazursky, J. E., Arrington, R. W., and Nogee, L. M. (2000) *Pediatr. Dev. Pathol. 3*, 335−345.
20. Weaver, T. E., and Beck, D. C. (1999) *Biol. Neonate 76 Suppl 1*, 15−8.
21. Glasser, S. W., Burhans, M. S., Korfhagen, T. R., Na, C. L., Sly, P. D., Ross, G. F., Ikegami, M., and Whitsett, J. A. (2001) *Proc. Natl. Acad. Sci. U.S.A. 98*, 6366−71.
22. Beck, D. C., Ikegami, M., Na, C. L., Zaltash, S., Johansson, J., Whitsett, J. A., and Weaver, T. E. (2000) *J. Biol. Chem. 275*, 3365−70.
23. Longo, M. L., Bisagno, A. M., Zasadzinski, J. A. N., Bruni, R., and Waring, A. J. (1993) *Science 261*, 453−456.
24. Lipp, M. M., Lee, K. Y. C., Waring, A., and Zasadzinski, J. A. (1997) *Biophys. J. 72*, 2783−804.
25. Lipp, M. M., Lee, K. Y. C., Takamoto, D. Y., Zasadzinski, J. A., and Waring, A. J. (1998) *Phys. Rev. Lett. 81*, 1650−1653.
26. Lipp, M. M., Lee, K. Y. C., Zasadzinski, J. A., and Waring, A. J. (1996) *Science 273*, 1196−9.
27. Ding, J., Takamoto, D. Y., von Nahmen, A., Lipp, M. M., Lee, K. Y. C., Waring, A. J., and Zasadzinski, J. A. (2001) *Biophys. J. 80*, 2262−72.
28. Waring, A., Taeusch, W., Bruni, R., Amirkhanian, J., Fan, B., Stevens, R., and Young, J. (1989) *Pept. Res. 2*, 308−13.
29. Bruni, R., Taeusch, H. W., and Waring, A. J. (1991) *Proc. Natl. Acad. Sci. U.S.A. 88*, 7451−7455.
30. Lee, K. Y. C., Majewski, J., Kuhl, T. L., Howes, P. B., Kjaer, K., Lipp, M. M., Waring, A. J., Zasadzinski, J. A., and Smith, G. S. (2001) *Biophys. J. 81*, 572−85.
31. Gupta, M., Hernandez-Juviel, J. M., Waring, A. J., and Walther, F. J. (2001) *Thorax 56*, 871−6.
32. Kumar, S. (1992) Conformational Analysis of a Synthetic Fragment of Lung Surfactant Apolipoprotein B, MS Thesis, University of Minnesota, Minneapolis, MN.
33. Jiarpinitnun, C. (2001) Biophysical Characterization of Lung Surfactant Protein B and its Mutant Engineered Peptides, BS Honors Thesis, University of Chicago, Chicago, IL.
34. Guermeur, Y., Geourjon, C., Gallinari, P., and Deleage, G. (1999) *Bioinformatics 15*, 413-21.
35. Guermeur, Y., Geourjon, C., Gallinari, P., and Deleage, G. (2001) http://npsa-pbil.ibcp.fr/cgi-bin/npsa_automat.pl?page=npsa_nn.html, Pôle Bio-Informatique Lyonnais−Institut de Biologie et Chimie des Protéines, Lyon, France.
36. Cuff, J. A., and Barton, G. J. (2000) *Proteins: Struct. Funct. Genet. 40*, 502−11.
37. Cuff, J. A., and Barton, G. J. (2000) http://jura.ebi.ac.uk:8888/, Barton Group, School of Life Sciences, University of Dundee, Dundee, U.K.
38. Gordon, L. M., Horvath, S., Longo, M. L., Zasadzinski, J. A., Taeusch, H. W., Faull, K., Leung, C., and Waring, A. J. (1996) *Protein Sci. 5*, 1662−75.
39. Gordon, L. M., Lee, K. Y. C., Lipp, M. M., Zasadzinski, J. A., Walther, F. J., Sherman, M. A., and Waring, A. J. (2000) *J. Pept. Res. 55*, 330−47.
40. Uematsu, N., and Matsuzaki, K. (2000) *Biophys. J. 79*, 2075−83.
41. Johansson, J., Szyperski, T., Curstedt, T., and Wuthrich, K. (1994) *Biochemistry 33*, 6015−23.
42. Bazzo, R., Tappin, M. J., Pastore, A., Harvey, T. S., Carver, J. A., and Campbell, I. D. (1988) *Eur. J. Biochem. 173*, 139−46.
43. Buckley, P., Edison, A. S., Kemple, M. D., and Prendergast, F. G. (1993) *J. Biomol. NMR 3*, 639−52.
44. Korzhnev, D. M., Bocharov, E. V., Zhuravlyova, A. V., Orekhov, V. Y., Ovchinnikova, T. V., Billeter, M., and Arseniev, A. S. (2001) *FEBS Lett. 495*, 52−5.
45. Armand, P., Kirshenbaum, K., Goldsmith, R. A., Farr-Jones, S., Barron, A. E., Truong, K. T., Dill, K. A., Mierke, D. F., Cohen, F. E., Zuckermann, R. N., and Bradley, E. K. (1998) *Proc. Natl. Acad. Sci. U.S.A. 95*, 4309−14.
46. Barchi, J. J., Huang, X. L., Appella, D. H., Christianson, L. A., Durell, S. R., and Gellman, S. H. (2000) *J. Am. Chem. Soc. 122*, 2711−2718.
47. Daura, X., Gademann, K., Schafer, H., Jaun, B., Seebach, D., and van Gunsteren, W. F. (2001) *J. Am. Chem. Soc. 123*, 2393−2404.
48. Jibson, M. D., and Li, C. H. (1981) *Int. J. Pept. Protein Res. 18*, 297−301.
49. Johansson, J., Szyperski, T., and Wüthrich, K. (1995) *FEBS Lett. 362*, 261−265.
50. Gesell, J., Zasloff, M., and Opella, S. J. (1997) *J. Biomol. NMR 9*, 127−35.
51. Jeener, J., Meier, B. H., Bachmann, P., and Ernst, R. R. (1979) *J. Chem. Phys. 71*, 4546−4553.
52. Macura, S., and Ernst, R. R. (1980) *Mol. Phys. 41*, 95−117.
53. Neuhaus, D., and Williamson, M. P. (2000) *The Nuclear Overhauser Effect in Structural and Conformational Analysis*, 2nd ed., Wiley-VCH, New York.
54. Cavanagh, J., Fairbrother, W. J., Palmer, A. G., Jr., and Skelton, N. J. (1996) *Protein NMR Spectroscopy: Principles and Practice*, Academic Press, Inc., San Diego, CA.
55. Wishart, D. S., Bigam, C. G., Yao, J., Adildgard, F., Dyson, H. J., Oldfield, E., Markley, J. L., and Sykes, B. D. (1995) *J. Biomol. NMR 6*, 135−140.
56. Piantini, U., Sorenson, O. W., and Ernst, R. R. (1982) *J. Am. Chem. Soc. 104*, 6800−6801.
57. Davis, D. G., and Bax, A. (1985) *J. Am. Chem. Soc. 107*, 2820−2821.
58. Rucker, S. P., and Shaka, A. J. (1989) *Mol. Phys. 68*, 509−517.
59. Shaka, A. J., Lee, C. J., and Pines, A. (1988) *J. Magn. Reson. 77*, 274−293.
60. Ogg, R. J., Kingsley, R. B., and Taylor, J. S. (1994) *J. Magn. Reson. B 104*, 1−10.
61. Maple, J. R., Dinur, U., and Hagler, A. T. (1988) *Proc. Natl. Acad. Sci. U.S.A. 85*, 5350−5354.
62. Dauber-Osguthorpe, P., Roberts, V. A., Osguthorpe, D. J., Wolff, J., Genest, M., and Hagler, A. T. (1988) *Proteins: Struct. Funct. Genet. 4*, 31−47.
63. Chen, Y.-H., Yang, J. T., and Chau, K. H. (1974) *Biochemistry 13*, 3350−3359.
64. Wüthrich, K. (1986) *NMR of Proteins and Nucleic Acids*, John Wiley & Sons, Inc., New York.
65. Wüthrich, K., Billeter, M., and Braun, W. (1984) *J. Mol. Biol. 180*, 715−40.
66. Wishart, D. S., Sykes, B. D., and Richards, F. M. (1992) *Biochemistry 31*, 1647−1651.
67. Merutka, G., Dyson, H. J., and Wright, P. E. (1995) *J. Biomol. NMR 5*, 14−24.
68. Berman, H. M., Westbrook, J., Feng, Z., Gilliland, G., Bhat, T. N., Weissig, H., Shindyalov, I. N., and Bourne, P. E. (2000) *Nucleic Acids Res 28*, 235−42.
69. Billeter, M., Schaumann, T., Braun, W., and Wuthrich, K. (1990) *Biopolymers 29*, 695−706.
70. Gong, Y., Zhou, H. X., Guo, M., and Kallenbach, N. R. (1995) *Protein Sci. 4*, 1446−56.
71. Identified by starting structure (x = extended strand, b = beta sheet, a = alpha helix), the most stable structures are as follows, in order: b, b, x, x, a, b, a, b, b, b, b, b, x, x, a, a, a.
72. Laskowski, R. A., MacArthur, M. W., Moss, D. S., and Thornton, J. M. (1993) *J. Appl. Crystallogr. 26*, 283−291.
73. Zhai, Y., and Saier, M. H., Jr. (2000) *Biochim. Biophys. Acta 1469*, 87−99.
74. Liepinsh, E., Andersson, M., Ruysschaert, J. M., and Otting, G. (1997) *Nat. Struct. Biol. 4*, 793−5.
75. Waring, A. J., Chen, Y., Faull, K. F., Stevens, R., Sherman, M. A., and Fluharty, A. L. (1998) *Mol. Genet. Metab. 63*, 14−25.
76. Kervinen, J., Tobin, G. J., Costa, J., Waugh, D. S., Wlodawer, A., and Zdanov, A. (1999) *EMBO J. 18*, 3947−55.
77. Osanai, K., Mason, R. J., and Voelker, D. R. (2001) *Biochim. Biophys. Acta 1531*, 222−229.
78. Baatz, J. E., Elledge, B., and Whitsett, J. A. (1990) *Biochemistry 29*, 6714−20.
79. Diamant, H., Witten, T. A., Gopal, A., and Lee, K. Y. C. (2000) *Europhys. Lett. 52*, 171−177.
80. Gopal, A., and Lee, K. Y. C. (2001) *J. Phys. Chem. B 105*, 10348−10354.

BI016077X